Optimization of CFTR gating through evolution of its extracellular loops

Condensed title: Gating differences between CFTR orthologues

Márton A. Simon[1,2,3*], László Csanády[1,2,3]

[1]Department of Biochemistry, Semmelweis University, Budapest, Hungary

[2]HCEMM-SU Molecular Channelopathies Research Group, Budapest, Hungary

[3]ELKH-SE Ion Channel Research Group, Budapest, Hungary

*For correspondence: ORCID: 0000-0002-5411-9408, simon.marton@med.semmelweis-univ.hu, 1094 Budapest Tuzolto utca 37-47.

Keywords: patch clamp, cystic fibrosis, R117H, zebrafish

Summary

In the human CFTR anion channel, an hR117-hE1124 H-bond stabilizes the bursting state, mutation hR117H causes cystic fibrosis. Instead, in zebrafish CFTR a zS109-zN120 H-bond stabilizes bursts through an alternative mechanism. Although serine and arginine are conserved, their interactions have evolved to increase open probability in hCFTR.

Abstract

CFTR chloride channel mutations cause the lethal and incurable disease cystic fibrosis (CF). CFTR is activated by phosphorylation, and phosphorylated channels exhibit 'bursting' behavior – 'bursts' of openings separated by short 'flickery' closures and flanked by long 'interburst' closures – driven by ATP binding/hydrolysis at two nucleotide-binding domains. The human channel (hCFTR) and the distant zebrafish orthologue (zCFTR) display differences both in their gating properties and structures. In phosphorylated, ATP-bound hCFTR the hR117 side chain, conserved across evolution, forms a H-bond which stabilizes the open state. Lack of that bond in the hR117H mutant causes CF. In the phosphorylated, ATP-bound zCFTR structure that H-bond is not observable. Here we show that the zR118H mutation does not affect function of zCFTR. Instead, we identify a H-bond between the zN120 and zS109 side chains of phosphorylated ATP-bound, but not unphosphorylated apo-zCFTR. We investigate the role of that interaction using thermodynamic mutant cycles, built on gating parameters determined in inside-out patch clamp recordings. We find that zS109 indeed forms a H-bond with zN120 in the flickery closed state, but not in the open or interburst closed states. Although in hCFTR an isoleucine (hI119) replaces the asparagine, mutation hS108A produces a strong hR117H-like phenotype. Because the effects of the latter two mutations are not additive, we conclude that in hCFTR these two positions interact, and the hS108-hR117 and hR117-hE1124 H-bonds cooperate to stabilize the open state. These findings highlight an example for how gating mechanism was optimized during CFTR molecular evolution.

Introduction

Cystic fibrosis (CF) is the most common inherited lethal disease in the Caucasian population. It is caused by loss-of-function mutations of the cystic fibrosis transmembrane conductance regulator (CFTR) anion channel, and results in the disruption of transepithelial salt-water transport in the lung, intestine, pancreatic duct and sweat duct (O'Sullivan and Freedman, 2009). The several hundred identified CF-causing mutations are divided into roughly six classes based on their effects on expression (class I), processing and trafficking (class II), channel gating (class III), anion permeation (class IV), and the amount and stability of the protein in the plasma membrane (classes V-VI.) (De Boeck and Amaral, 2016). Although CF is currently incurable, recent development of small-molecule drugs that target the CFTR protein marked a milestone, complementing traditional symptomatic treatment. A significant symptomatic improvement is observed for CF patients with class III mutations when treated with the 'potentiator' drug Vx-770 (ivacaftor) which overcomes gating defects (Ramsey *et al.*, 2011), and for class II patients when treated with Trikafta, a combination of Vx-770 with two 'corrector' drugs that facilitate protein folding (Heijerman et al., 2019; Sutharsan et al., 2022; Middleton et al., 2019; Barry et al., 2021) Because the effects of these small-molecule drugs on different mutants are greatly variable, understanding the underlying molecular background of each CF-causing mutation is of great clinical significance.

CFTR belongs to the superfamily of ATP-binding cassette (ABC) proteins and consists of two transmembrane domains (TMD1/2; Fig 1A-C, gray), two cytosolic nucleotide-binding domains (NBD1/2; Fig 1A-C, blue and green, respectively) and a cytosolic regulatory (R) domain unique to CFTR (Fig 1A, pale magenta) which links the two ABC-typical TMD-NBD halves together (Fig 1A) (Riordan *et al.*, 1989) and must be phosphorylated to allow channel activity (Cheng *et al.*, 1991).

In phosphorylated channels binding of ATP to the 'head' of each NBD promotes formation of a head-to-tail NBD dimer which occludes two ATP molecules in composite interfacial binding sites (sites 1 and 2), one of which (site 2) possesses ATPase activity. NBD dimerization is coupled to TMD movements that resemble the rearrangement of ABC exporter proteins from an inward-facing (IF) to an outward-facing (OF) (Fig 1B-C) orientation ((Liu et al., 2017; Zhang et al., 2018b); reviewed, e.g., in (Csanády *et al.*, 2019)). Phosphorylated CFTR channels in the presence of ATP exhibit bursting behavior:

bursts of openings (to state O) separated by short 'flickery' closures (to state C_f) are flanked by long 'interburst' closures (to state C_s). State C_s corresponds to an IF TMD orientation (Bai et al., 2011; Wang et al., 2014) with a closed channel pore and at least partially separated NBDs (Vergani et al., 2005; Tsai et al., 2010). The burst state (B) is a composite state that includes the O and C_f states and exhibits an OF TMD conformation (Bai et al., 2011; Wang et al., 2014) associated with a tight, ATP-occluded NBD dimer (Vergani *et al.*, 2005). For wild-type (WT) CFTR, this highly stable B state is terminated usually by the hydrolysis of ATP at site 2, which leads to the dissociation of the NBD dimer and resets the TMDs to the IF orientation (Csanády *et al.*, 2010). Of note, the currently available cryo-electronmicroscopy (cryo-EM) structures of IF and OF CFTR (PDB: 5UAK, 6MSM) are not precise representations of the C_s and B states, respectively, as the former was obtained from unphosphorylated CFTR in the absence of ATP, while in the latter structure the external end of the pore is too narrow to accommodate a hydrated chloride ion. Nevertheless, to date, these structures are the best available models for gating-associated conformational changes of the channel pore.

In unphosphorylated CFTR the pore is closed (IF), and the R domain is wedged between the NBDs (Liu *et al.*, 2017) preventing their dimerization. Upon activation, cAMP-dependent protein kinase (PKA) binds to the R domain (Mihályi *et al.*, 2020), and in the presence of ATP phosphorylates multiple serines (Cheng *et al.*, 1991), leading to the release of the R domain from its inhibitory intercalated position (Zhang *et al.*, 2018b).

CFTR is a vertebrate-specific anion channel, the most ancient identified orthologue to date is found in the sea lamprey (Cui *et al.*, 2019). Although all CFTR orthologues show a considerable degree of sequence homology, alterations in channel mechanics of different CFTRs are observable compared to human CFTR (hCFTR), one of the current endpoints of CFTR molecular evolution. The extensively studied zebrafish CFTR (zCFTR) is among the most ancient orthologues, and might serve as a relatively early representative of CFTR development. Compared to hCFTR, the open probability (P_o) of zCFTR is drastically reduced, resembling that of hCFTR harboring the CF-causing mutation R117H (Zhang *et al.*, 2018a). The available high-resolution structures of hCFTR and zCFTR, solved by cryo-EM, have shed light onto structural differences that provide invaluable insight into understanding the structural development that has

occurred during CFTR molecular evolution. While the IF structures of the two orthologues (hCFTR PDB: 5UAK; zCFTR PDB: 5UAR) are closely similar (Zhang and Chen, 2016; Liu et al., 2017), the two OF structures (hCFTR PDB: 6MSM, Fig 1B; zCFTR PDB: 5W81, Fig 1C) show distinct differences. In OF hCFTR the external end of the pore is open (though not wide enough to allow a hydrated chloride ion to permeate), whereas in OF zCFTR it is tightly closed. Furthermore, the positions of the NBDs at site 1 and the arrangement of the extracellular loops in the two OF structures differ to some extent (Zhang et al., 2017; Zhang et al., 2018b). Understanding how CFTR gating mechanism was optimized through its structural evolution might provide important insight into CFTR structure-function.

In hCFTR the hR117 side chain in the first extracellular loop (ECL1) plays a critical role in stabilizing the O state by forming a H-bond with the backbone carbonyl group of hE1124 in ECL6, suggested by the OF hCFTR structure (Fig 1D) and confirmed by functional studies (Simon and Csanády, 2021). Lack of that stabilizing interaction in the class III mutant hR117H dramatically reduces P_o (Sheppard et al., 1993; Yu et al., 2016) and causes CF (Dean et al., 1990; Wilschanski et al., 1995). Interestingly, a H-bond between the corresponding positions (zR118-zD1132) is not observable in the OF zCFTR structure (Fig 1E): the zR118-zD1132 α-carbon distance is too large, and the zR118 side chain is resolved only to the β-carbon atom, likely due to increased side chain flexibility. Based on these structural observations one possible explanation for the reduced P_o of WT zCFTR might be that the stabilizing interaction of zR118 never forms during gating of zCFTR, resulting in an hR117H-like phenotype. Alternatively, considering that the arginine is evolutionarily highly conserved, the absence of the stabilizing zR118-zD1132 interaction in the OF zCFTR structure might be explained by assuming that the latter represents the C_f, rather than the O state. To address this functional question, we aimed to test the effect of the zR118H mutation on zCFTR gating using inside-out patch clamp recordings. Furthermore, our purpose was to deconvolve the structural correlates of evolutionary changes in CFTR gating mechanisms.

Materials and methods

Reagents

NaCl (27800.291) and HEPES (441476L) were purchased from VWR Chemicals, KCl (P4504-1KG), $MgCl_2$ (M1028-100ML), NaOH (S8045-1KG), $CaCl_2$ (21115-250ML), NMDG (M2004-500G), EGTA (03777-10G), were purchased from Sigma Aldrich, HCl was purchased from Supleco.

Molecular biology

The zCFTR coding sequence was subcloned into the XmaI and SalI sites of pGEMHE. Mutations were introduced into the hCFTR-E1371S (pGEMHE) and zCFTR-E1372S (pGEMHE) sequences using the QuikChange II XL Kit (#200521, Agilent Technologies) and confirmed by Sanger sequencing (LGC Genomics GmbH). To generate cRNA, the cDNA was linearized (NheI-HF, R3131 S, New England Biolabs) and transcribed in vitro using T7 polymerase (mMessage mMachine T7 Kit, AM1344, ThermoFisher Scientific), cRNA was stored at –80°C.

Functional expression of CFTR constructs in Xenopus laevis oocytes

Oocytes were removed by surgery from anesthetized *Xenopus laevis* following Institutional Animal Care Committee guidelines, and separated by collagenase treatment (Collagenase type II, 17101015, Gibco). Isolated oocytes were kept at 18°C, in a modified frog Ringer's solution (82 mM NaCl, 2 mM KCl, 1 mM $MgCl_2$, and 5 mM HEPES, pH 7.5 with NaOH) supplemented with 1.8 mM $CaCl_2$ and 50 μg/ml gentamycin (G1397-10mL, Sigma). Injections by 0.1–10 ng of cRNA, to obtain microscopic or macroscopic currents, were done in a fixed 50 nl volume (Nanoject II, Drummond). Recordings were performed 1–3 days after injection.

Functional expression of CFTR constructs in HEK-293T cells

HEK-293T Cells were cultured at 37°C in 5% CO_2 in Dulbecco's Modified Eagle's Medium (DMEM) with 4.5 g/L glucose (Lonza), supplemented with 10% Fetal Bovine Serum (FBS) (EuroClone), 2 mM L-glutamine, and 100 units/ml penicillin/streptomycin (Lonza). HEK-293T cells transiently expressing CFTR and green fluorescent protein (GFP) were obtained by cotransfection of HEK-293T cells with a given CFTR-pcDNA3 construct and GFP-pcDNA3 at a 10:1 ratio (FuGENE HD transfection reagent, Promega). Measurements were performed 1-2 days after transfection.

Excised inside-out patch recording

The patch pipette solution contained 138 mM NMDG, 2 mM $MgCl_2$, 5 mM HEPES, pH 7.4 with HCl. The bath solution contained 138 mM NMDG, 2 mM $MgCl_2$, 5 mM HEPES, 0.5 mM EGTA, pH 7.1 with HCl. Following excision into the inside-out configuration patches (each from a different cell to enhance biological variability) were moved into a flow chamber in which the composition of the continuously flowing bath solution could be exchanged with a time constant of <100 ms using electronic valves (ALA-VM8, Ala Scientific Instruments). CFTR channel gating was studied at 25°C, in the presence of 2 mM MgATP (A9187-1G, Sigma), following activation by ~1 min exposure to 300 nM bovine PKA catalytic subunit (P2645, Sigma; activation time constants were <20 s for each construct). Macroscopic currents were recorded at -20 / -40 / -80 mV, microscopic currents at –80 / -120 mV membrane potential. Currents were amplified and low-pass filtered at 2 kHz (Axopatch 200B, Molecular Devices), digitized at a sampling rate of 10 kHz (Digidata 1550B, Molecular Devices) and recorded to disk (Pclamp 11, Molecular Devices).

Kinetic analysis of electrophysiological data

Relaxation time constants (τ_b; Figs. 2B, 3B,D, 4B, 5E, 6B, 7E, S2B) were obtained by fitting macroscopic current relaxations to single exponentials using non-linear least squares (Clampfit 11).

For intraburst kinetic analysis ATP was briefly added to open prephosphorylated channels, and was then removed. Segments of record following the last observed superimposed channel opening were analyzed (highlighted by black horizontal lines in Figs. 2C, 5A, 6D, 7A). Mean open times (τ_o) and mean flickery closed times (τ_f) were obtained as the simple arithmetic averages of the mean open and closed dwell-time durations, respectively, and $K_{eq|B}$ was calculated as $K_{eq|B}=\tau_{open}/\tau_{flicker}$ (Figs. 2D, 5B, 6E, 7B). Of note, for low-P_o constructs this approach does not eliminate the possibility that two channels are still active during some initial part of the analyzed segment even if they do not open simultaneously. However, such a scenario predicts a sudden irreversible drop in apparent P_o, at the time point of final closure of the last-but-one channel somewhere within the analyzed segment. Because we did not observe such trends upon visual inspection, we believe that for each of the studied constructs the majority of total "last-

channel" recording time must have indeed documented gating of a single active channel. I.e., a potential overestimation of intraburst P_o should be minimal.

Mutant cycle analysis

Changes in the strengths of the zS109 – zN120, zS109-zR118, hS108 – hR117 and hS108-hN119 interactions between various gating states were evaluated using thermodynamic mutant cycle analysis as described previously. Briefly, for an $S_1 \leftrightarrow T^{\ddagger} \leftrightarrow S_2$ gating step changes in the relative stabilities of those three states induced by a particular mutation were calculated as follows. The change in the height of a transition-state barrier, such as for step $S_1 \rightarrow T^{\ddagger}$, was calculated as $\Delta\Delta G^0_{T\text{-}S1} = -kT\ln(r'_{12}/r_{12})$, where k is Boltzmann's constant, T is absolute temperature, and r_{12} and r'_{12} are the rates for the $S_1 \rightarrow S_2$ transition in the background construct and in the mutant, respectively. The change in the stability of the two ground states relative to each other was calculated as $\Delta\Delta G^0_{S2-S1} = -kT\ln(K'_{eq}/K_{eq})$, in which K_{eq} and K'_{eq} are the equilibrium constants for the $S_1 \leftrightarrow S_2$ transition in the background construct and in the mutant, respectively. Interaction free energy ($\Delta\Delta G_{int}$) was defined as the difference between $\Delta\Delta G^0$ values along two parallel sides of a mutant cycle. All $\Delta\Delta G$ values are given as mean ± SEM; SEM values were estimated assuming that r_{ij} and K_{eq} are normally distributed random variables, using second-order approximations of the exact integrals (Mihályi *et al.*, 2016).

Statistics

All values are given as mean ± SEM, with the numbers of independent samples provided in each figure legend. Data distribution was assumed to be normal, but this was not formally tested. Statistical significances of interaction free energies were calculated using Student's t two-tailed test, $\Delta\Delta G_{int}$ is reported significantly different from zero for $p < 0.05$.

Sequence alignment

Sequences of CFTR orthologues were obtained using NCBI blast, by providing the protein sequence of hCFTR (UniProt: P13569) for search in the non-redundant protein database. Sequences were manually curated, and then aligned using the clustalW algorithm. Sequences to display in the sequence alignment (Fig. S1) were selected based on a simplified phylogenetic tree of CFTR molecular evolution (Infield et al., 2021).

Online supplemental material

Fig S1 provides a sequence alignment that illustrates the molecular evolution of ECL1 in CFTR. Fig S2 shows the assessment of a potential link between residues zS109 and zR118 in the zCFTR orthologue.

Results

Non-hydrolytic zCFTR background construct zE1372S exhibits lower intraburst P_o but similar burst duration when compared to human orthologue

In WT CFTR channels pore closure can happen along two pathways: NBD dimer dissociation may follow hydrolysis of ATP at site 2 or may occur occasionally in the absence of ATP hydrolysis. Thus, mutational effects on open-state stability are difficult to interpret. Mutations of the Walker B glutamate side chain in NBD2 (e.g., hE1371S/ zE1372S) prevent ATP hydrolysis. Such "non-hydrolytic" mutations prolong the mean burst duration (τ_{burst}) by more than two orders of magnitude and reduce CFTR gating in saturating ATP to reversible $C_s \leftrightarrow B$ transitions (Csanády *et al.*, 2010). For such channels the slow rate of the non-hydrolytic $B \rightarrow C_s$ transition can be measured in macroscopic inside-out patch clamp recordings by activating prephosphorylated channels with exposure to ATP (2 mM for 1 min), followed by sudden ATP removal. Fitting the resulting slow current decay time courses (Fig. 2A, black and gray traces) with exponentials the obtained time constant reports the average lifetime of the B state under non-hydrolytic conditions (τ_{burst}; Table 1, Fig. 2B, black and gray bars). Using that approach, we determined τ_{burst} for both hE1371S (Fig. 2A, black trace; Fig. 2B black bar) and zE1372S (Fig. 2A, gray trace; Fig. 2B gray bar), the two background constructs used in this study. We found that mean burst duration is slightly, but not significantly ($p=0.071$) longer for zE1372S (57 ± 8.3 s, n=9, biological replicates) than for hE1371S (37 ± 3.7 s, n=7, biological replicates), consistent with formation of a stable NBD dimer already in the zebrafish orthologue.

The B state is a compound state, consisting of the O and C_f states. As the burst is prolonged in the hE1371S and zE1372S backgrounds, it is possible to inspect large numbers of openings and flickery closings without any interburst event by observing the last open channel following ATP removal – under such conditions gating continues until

the first transition to the interburst closed state from which the probability of reopening is extremely low in the absence of ATP (Simon et al., 2021). This allows studying effects on intraburst P_o ($P_{o|B}$) or the intraburst closed – open equilibrium constant ($K_{eq|B} = P_{o|B} / (1-P_{o|B})$). Comparing gating of last open channels for the hE1371S (Fig. 2C, black trace) and zE1372S (Fig. 2C, gray trace) background constructs, a large difference in intraburst P_o values is immediately evident: the calculated $K_{eq|B}$ values (Table 1, Fig. 2D, black symbol – hE1371S, gray symbol – zE1372S) show a striking ~54-fold difference between the two orthologues. In summary, under non-hydrolytic conditions intraburst kinetics of zE1372S resembles that of hR117H, but the B state of zE1372S seems as stable as that of hE1371S.

Different substitutions of the catalytic glutamate differentially affect burst stability in zCFTR and hCFTR

Our finding of a reduced intraburst P_o for zE1372S compared to hE1371S, obtained in patches excised from *Xenopus laevis* oocytes, is in agreement with an earlier report which compared zE1372Q and hE1371Q channels expressed in mammalian cell membranes (Zhang *et al.*, 2018a). On the other hand, the similar burst durations of zE1372S and hE1371S seem to contrast with the findings of the earlier study which reported ~4-fold shorter τ_{burst} for zE1372Q compared to hE1371Q.

To evaluate the possibility that membrane composition might influence the stability of NBD dimers, we performed similar experiments on CFTR channels expressed in HEK293T mammalian cells instead of our *Xenopus* laevis oocyte model system (Fig. 3A; brown trace – hE1371S, pale brown trace – zE1372S) and determined τ_{burst} (Fig. 3B, colored bars). However, we found no significant difference either in τ_{burst} of hE1371S ($p=0.42$) or in τ_{burst} of zE1372S ($p=0.091$) between the two expression systems.

To evaluate the alternative possibility that the different substitutions used in the two studies underlie the seemingly discrepant results, we constructed hE1371Q and zE1372Q and assessed their mean burst durations in our oocyte based model system. Surprisingly, replacement of the catalytic glutamate with a glutamine resulted in bursts which for hCFTR were >10-fold longer, but for zCFTR not significantly longer ($p=0.092$), compared to those of the respective serine mutants ((Fig. 3A vs. 3C, black and

gray traces; Fig. 3B vs. 3D, black and gray bars). As a consequence, τ_b was ~6-fold shorter for zE1372Q compared to hE1371Q (Fig. 3C-D), consistent with the earlier report (Zhang *et al.*, 2018a). Thus, different substitutions of the catalytic glutamate differentially affect burst stability in zCFTR and hCFTR, suggesting important differences in the network of interdomain interactions that stabilize the NBD dimer interface. Whereas identification of the source of these differences is beyond the scope of the present work, these findings underscore the importance of employing a single non-hydrolytic background construct for the evaluation of energetic effects of second-site mutations. In the present study, the serine mutants were chosen as the background for both orthologues.

Mutation R118H in zCFTR produces no functional phenotype

We next examined the effect of the zR118H mutation on the gating of zCFTR (Fig. 4A, pale blue trace). Surprisingly, unlike the acceleration caused by mutation hR117H in the hCFTR background (hE1371S) (Fig. 4A, black vs. dark blue trace), in the zCFTR background (zE1372S) the zR118H mutation did not result in an R117H-like acceleration of the current decay (Fig. 4A, gray vs. pale blue trace). Consistently, analysis of fitted τ_{burst} values (Table 1, Fig. 4B, colored bars) reported a slight, but statistically not significant ($p = 0.27$) ~1.3-fold increase in τ_{burst} for zR118H compared to zE1372S, instead of a ~4-fold decline predicted based on the effect of the analogous mutation on hE1371S. Because at our recording bandwidth the unitary amplitude of last channel currents was smaller than 0.3 pA at -120 mV (0.6 pA for zE1372S), intraburst kinetics could not be examined reliably.

Outward-facing zCFTR structure suggests alternative stabilizing interaction within ECL1

Because the bursting state in zE1372S is as stable as that of hE1371S (Fig. 4B, black vs. gray bar) but τ_{burst} is not shortened by mutation zR118H, an alternative stabilizing interaction – which does not involve the zR118 side chain – must be present in zCFTR. Therefore, we examined the extracellular region of the OF zCFTR structure in greater depth, searching for an interaction between ECL1 – ECL6 which is absent in all other CFTR structures (IF zCFTR, IF / OF hCFTR). Interestingly, we discovered a H-bond between the side chains of zS109 and zN120 (Fig. 4D), which might potentially serve to stabilize ECL1. This interaction is absent in the IF zCFTR structure (Fig. 4F), as

well as in all hCFTR structures (Fig. 4C, 3E) in which the serine is conserved (hS108) but the asparagine is replaced by an isoleucine (hI119). Moreover, for the latter position a clear evolutionary trend is observable based on sequence alignment (Fig. S1): a polar amino acid present in more ancient organisms (e.g. E in sea lamprey, N/Q in most fishes) is replaced by a hydrophobic residue in later orthologues (e.g., I in mammals). However, because of the limited resolution of these extracellular regions in both electrondensity maps (EMD-9230, EMD-8782), and the typically poor cryo-EM signal of charged side chains in general, these modeled side-chain interactions must be interpreted with caution, unless their existence is functionally verified. We thus aimed to test the validity and functional relevance of the putative H-bond between positions z109-z120.

Intriguingly, in the OF hCFTR structure (Fig. 4C) the modeled backbone carbonyl group of hS108 forms a H-bond with the δ-amino group of the hR117 side chain, suggesting functional coupling between the two positions (hS108 – hR117). Thus, we also aimed to verify the functional role of position hS108 in the human orthologue.

The zS109 – zN120 interaction stabilizes the flickery closed state in zCFTR

The functional impact of a mutation at a certain position of a protein depends on the whole interactome of that specific residue, as one amino acid often takes part in multiple interactions, all of which are perturbed upon mutagenesis. To isolate and quantify the energetic effect of altering a single specific interaction between two target residues, thermodynamic mutant cycle analysis must be applied (Fersht, 2002; Vergani et al., 2005). For that purpose, a thermodynamic cycle is formed by the background construct, two single-mutant constructs, each perturbing one participant of the selected interaction, and a double-mutant containing both mutations at the selected positions. If the interaction of the target residues changes between two gating (ground / transition) states (S_1, S_2), then the impact on relative stability of state S_2 ($\Delta\Delta G^{\circ}_{S2\text{-}S1}$) caused by perturbing one target residue depends on the nature of the side chain present at the other target position: thus, the energetic effects of each single mutation are not additive in the double mutant. By contrast, additive effects of the single mutations signal that the interaction is not present or does not change between the S_1 and S_2 gating states. The change in interaction energy of the target interaction between the two gating states

($\Delta\Delta G_{int}$ ($S_1 \rightarrow S_2$)) is calculated as the difference of $\Delta\Delta G^{\circ}_{S2\text{-}S1}$ values along two parallel sides of the mutant cycle (Fig. 5C).

To study how the zS109-zN120 interaction changes during intraburst gating, we extracted the intraburst equilibrium constant (Fig. 5B, colored symbols) from records of last open channels (Fig. 5A, colored traces) for zE1372S, and for the zN120A, zS109A, and zS109A-zN120A mutants constructed in the same background. The zN120A mutation increased $K_{eq|B}$ by ~7-fold when introduced into the background construct (Table 1, Fig. 5A-B, gray vs. magenta), but not when introduced into the zS109A background (Fig. 5A-B, orange vs. green). The calculated change in interaction energy between positions zS109 and zN120 during step $C_f \rightarrow O$ is +2.7 ± 0.46 kT (Fig. 5C, purple; k, Boltzmann's constant; T, temperature). That value is similar to the average energy of a H-bond (~2-3 kT), and its positive signature is consistent with a stabilizing interaction selectively present in state C_f, confirming the assumed H-bond between the target positions. As the S109-N120 interaction is present only in the C_f state and is absent in the O state, the phosphorylated, OF zCFTR structure must represent the C_f, rather than the O state.

Next, we investigated how the strength of the zS109-zN120 interaction changes while the channel proceeds from the bursting state (B) to the transition state for interburst closure ($T^{\ddagger}$), by comparing τ_{burst} of our background construct (zE1372S), single mutants zS109A and zN120A, and the corresponding double mutant (Fig. 5D, colored traces, Table 1, Fig. 5E, colored bars). Both single mutations decreased τ_{burst}, consistent with overall destabilization of the bursting state by the mutations, but these effects were largely additive. E.g., the zS109A mutation decreased τ_{burst} by ~ 3-fold, regardless of whether it was introduced into the zCFTR background (Fig. 5D-E, gray vs. orange) or into zN120A (Fig. 5D-E, magenta vs. green). The similar changes in $\Delta\Delta G^{\circ}_{T\ddagger\text{-}B}$ along two parallel sides of the mutant cycle (Fig. 5F, numbers on vertical arrows) resulted in a $\Delta\Delta G_{int}$ value close to zero for the $B \rightarrow T^{\ddagger}$ gating step (Fig. 5F, purple). This suggests that the interaction is either not present or static between the two states. As the zE1372S background construct spends the majority of the burst in the C_f state (Fig. 5A-B, gray) in which the target interaction is formed, it is assumed that the interaction is maintained in

the $T^{\ddagger}$ state (but is likely absent in the C_s state, as it is not observed in the IF zCFTR structure).

Of note, whereas single mutation zN120A shifted the C_f – O equilibrium towards the O state (Fig. 5B, gray vs. magenta), as expected for disruption of an interaction that stabilizes the C_f state, single mutation zS109A rather decreased $K_{eq|B}$ (Fig. 5B, gray vs. orange). This suggests that besides its interaction with zN120, zS109 is also involved in a strong stabilizing interaction, which is formed in the O state, with an unknown residue different from zN120. Disruption of both of these interactions in the zS109A mutant would explain on one hand the lack of a net effect on $K_{eq|B}$, and on the other hand the much larger effect on τ_{burst} (Fig. 5E, magenta vs. orange), of the zS109A single mutation.

In hCFTR hS108 cooperates with hR117 to stabilize the O state

Although the hydrophilic residue corresponding to zN120 is replaced by a hydrophobic isoleucine in higher eukaryotes, the serine corresponding to zS109 is conserved throughout evolution (Fig. S1). Moreover, in the OF hCFTR structure a potential H-bond is observable between the backbone carbonyl group of the latter position (hS108) and the δ-amino group of hR117 (Fig. 4C). We therefore examined if residue hS108 plays any role in hCFTR gating. To attempt to perturb the position of its backbone carbonyl group, we truncated the side chain of hS108, which is involved in stabilizing the terminal portion of transmembrane helix 1 (TM1).

We first studied macroscopic current relaxations upon ATP removal (Fig. 6A) to extract mean burst durations (Table 1, Fig. 6B). Interestingly, mutation hS108A decreased τ_{burst} ~3-fold compared to the hE1371S construct (Fig. 6A-B, black vs. orange). As mutation hR117H affected τ_{burst} in a similar way (Fig. 6A-B, black vs. blue), we constructed the double mutant, to address additivity between the two positions. Introducing mutation hS108A into an hR117H background increased τ_{burst} by ~ 2-fold (Fig. 6A-B, blue vs. green), revealing strong coupling between positions hS108 and hR117. The extent of this coupling, quantified by the thermodynamic mutant cycle, amounts to $\Delta\Delta G_{int}$ ($B \rightarrow T^{\ddagger}$) = 1.9 ± 0.20 kT (Fig. 6C; purple), confirming the existence of the potential H-bond in the bursting state.

Next, we studied the change in hS108-hR117 interaction energy between C_f and O states, by quantifying mutational effects on the intraburst gating equilibrium (Fig. 6E) extracted from records of last open channels (Table 1, Fig. 6D). Introduction of mutation hS108A decreased $K_{eq|B}$ dramatically, by ~70-fold, compared to the background (Fig. 6D-E, black vs. orange), again mimicking the hR117H phenotype (Fig. 6D-E, black vs. blue). To complete the thermodynamic mutant cycle, we studied the effect of the hS108A mutation also in the hR117H background, and found that it resulted in an only ~4-fold decrease in $K_{eq|B}$ (Fig. 6D-E, blue vs. green). The magnitude of the calculated $\Delta\Delta G_{int}$ ($C_f \rightarrow O$) = -2.9 ± 0.47 kT (Fig. 6F; purple) is comparable to the strength of a H-bond, and its negative signature implies that within the B state the H-bond between positions hS108 and hR117 is present in the O state but not in the C_f state.

We also examined whether a potential link might exist also in zCFTR between zS109 and zR118. For that purpose, mutation zR118H was introduced into the zS109A construct (Fig. S2A, green trace), and τ_{burst} was determined as described above (Table 1, Fig. S2B, green bar). Although the two single mutations zS109A and zR118H exerted inverse effects on τ_{burst} of the zE1372S background (Table 1, Fig. S2B, blue and orange vs. gray), their effects in the double mutant proved additive (Fig. S2A, green vs. gray). The calculated $\Delta\Delta G_{int}$ value was 0.43 ± 0.26 kT (Fig. S2C, purple), which is not significantly different from zero ($p = 0.14$). Therefore, no coupling is present between the zR118 and zS109 residues in the zebrafish orthologue.

In hCFTR the ancient interaction which stabilizes the C_f state can be restored

Although at the position corresponding to zN120 replacement of the polar residue (N/Q/E) by an isoleucine happened relatively early in CFTR evolution, we were curious whether such an interaction can be restored in later orthologues. Therefore, we introduced the hI119N mutation into our hCFTR background (hE1371S) and examined its potential interaction with hS108 by deducing the $K_{eq|B}$ (Table 1, Fig. 7B, colored symbols) from last open channel recordings (Fig. 7A, colored traces).

The hI119N mutation decreased $K_{eq|B}$ by ~17-fold when introduced into the background construct (Fig. 7A-B, black vs. magenta), but only by ~3.5-fold when introduced into the hS108A background (Fig. 7A-B, orange vs. green), suggesting non-

additive effects of the two mutations. In order to correctly interpret these data, it has to be considered that the postulated H-bond may exist only in the hI119N mutant, which contains both the hS108 and the hN119 target side chain. Thus, following conventional mutant cycle formalism this construct should be considered the 'background' (Fig. 7C, top left corner), whereas constructs hE1371S (only hS108 present) and hS108A-I119N (only hN119 present) should be considered 'single mutants' (Fig. 7C, top right and bottom left corners), and construct hS108A (neither hS108 nor hN119 present) the 'double mutant' (Fig. 7C, bottom right). The calculated change in interaction energy between positions hS108 and hN119 of the hI119N construct during step $C_f \rightarrow O$ is +1.6 ± 0.38 kT (Fig. 7C, purple). That value is comparable to the average energy of a H-bond (~2-3 kT), and its positive signature is consistent with a stabilizing interaction present in state C_f, similar to the zS109-zN120 interaction (Fig. 5A-C). Thus, the H-bond between positions h108 and h119, lost over evolution, is restored in the hI119N mutant.

Next, we examined macroscopic current relaxations upon removing ATP (Fig. 7D, colored traces) to deduce τ_{burst} values (Table 1, Fig. 7E, colored bars). Mutation hI119N increased τ_{burst} slightly, by ~1.5-fold, when introduced into the hE1371S background construct (Fig. 7D-E, black vs. magenta), but by 2.5-fold, when introduced into construct hS108A (Fig. 7D-E, orange vs. green). The change in interaction energy quantified by the thermodynamic mutant cycle is -0.64 ± 0.26 kT (Fig. 7F, purple), which is small, but significantly different from zero ($p = 0.042$). That small but negative $\Delta\Delta G$ reports a small increase in the strength of the H-bond in the hI119N channel as it transits from the B state to the $T^{\ddagger}$ state. Because during a burst the H-bond forms only in state C_f, and hI119N channels spend ~50% of the burst-time in that state (Fig. 7B, magenta symbol), the time-average of the interaction energy within a burst amounts to ~half of that of an H-bond. Thus, the apparent further small stabilization of the interaction in state $T^{\ddagger}$ suggests that the H-bond is formed in the $T^{\ddagger}$ state. In contrast, based on modeling of the hI119N mutant by Missense3D, no interaction is present between the target positions in the IF state, thus, the hS108-hN119 interaction is likely to be absent in state C_s. These data together suggest that in the hI119N construct the restored H-bond between hS108 and hN119 stabilizes the C_f state, but is absent in the O and C_s states, similarly to the zS109-zN120 interaction natively present in the zebrafish orthologue.

Discussion

The NBD-dimerized OF conformation of the CFTR channel corresponds to the 'bursting' state within which the ion-conducting pore alternates between fully open (O) and flickery closed (C_f) states. For human CFTR the bursting state is highly stable: when ATP hydrolysis is prevented τ_{burst} is increased by >100-fold, from ~0.2 s (Csanády et al., 2010) to ~37 s (Fig. 3B, black) or ~470 s (Fig. 3D, black), depending on the catalytic site mutation employed. The mutation-specific variations in non-hydrolytic burst duration clearly indicate that, in addition to disrupting ATP hydrolysis, different catalytic site mutations differentially affect the stability of the prehydrolytic NBD dimer. Nevertheless, regardless of which mutant most closely resembles the prehydrolytic state of a WT channel, the >100-fold difference in hydrolytic and non-hydrolytic closing rates indicates that in WT hCFTR the vast majority of bursts is terminated by ATP hydrolysis (cf., (Csanády et al., 2010)). In that regard, the bursting state itself is comparably stable in the zebrafish orthologue: given the reported τ_{burst} of ~0.7 s of WT zCFTR (Zhang et al., 2018a), the observed ~100-fold longer τ_{burst} of non-hydrolytic mutants (Fig. 2B, 2D gray) reports that the gating (burst-interburst) cycle is strictly coupled to ATP hydrolysis already in the zebrafish orthologue. On the other hand, for human CFTR the bursting state is also highly conductive: within a burst the pore is open for ~95% of the time (intraburst P_o is ~0.95; cf., Fig. 2D, black). In contrast, the intraburst P_o of zCFTR is much lower (~0.29, Fig. 2D, gray; cf. (Zhang *et al.*, 2018a)). Thus, from the point of view of ion conduction, zCFTR is a 'less efficient' ion channel, which was greatly optimized in the course of evolution.

Cryo-EM structures of hCFTR and zCFTR are highly similar in both IF and OF conformations, but show marked differences in the arrangement of extracellular loops (Zhang et al., 2017; Zhang et al., 2018b), a region known to have a strong impact on intraburst P_o by contributing interactions that stabilize the NBD-dimerized OF conformation (Cui et al., 2014; Infield et al., 2016; Yu et al., 2016). Inspection of these structures provided a good starting point for identifying functionally relevant state-dependent interactions that differ for zCFTR and hCFTR (Fig. 4C-F) and are formed between conserved or systematically evolving positions (Fig. S1). However, because the

resolution of the cryo-EM maps is poor in this region, the relevance of these suggested interactions must be validated by functional studies. In particular, an earlier functional study showed that in hCFTR a strong H-bond between the side chain of hR117 in ECL1 and ECL6-residue hE1124 (Fig. 1D), selectively present in the O state, is required both for the stable bursting state and the high intraburst P_o characteristic of hCFTR: mutations of hR117 dramatically impair channel gating and cause CF (Simon et al., 2021). Here, we show that despite its high conservation throughout evolution (Fig. S1), the ECL1 arginine does not play such a stabilizing role in the ancient zCFTR orthologue, as its mutation does not produce a phenotype (Fig. 4A-B, gray vs. light blue). Instead, based on the OF zCFTR structure, we identify here zN120 and zS109, located at the extracellular ends of TM1 and TM2, respectively, and show that they play a pivotal role in burst stabilization: truncation of their side chains shorten τ_{burst} (Fig. 5D-E, gray vs. magenta and orange). Interestingly, however, intraburst P_o is oppositely affected by these mutations (Fig. 5A-B, gray vs. magenta or orange), suggesting that the zN120 and zS109 side chains are differentially involved in stabilizing the O and the C_f state. We further show here that these effects involve state-dependent interactions of zS109 with two distinct residues (cartooned in Fig. 8, upper panel). A H-bond with zN120, located at the extracellular end of TM2, is selectively formed in state C_f (Fig. 5C). Because that bond is visible in the OF zCFTR structure, we conclude that the latter must represent a flickery closed state. In contrast, identification of the open-state interaction partner of zS109 (question mark in Fig. 8, upper panel) will require an open zCFTR structure.

Although zCFTR cannot be considered a direct predecessor of hCFTR, a clear evolutionary tendency can be observed for the residue corresponding to zN120: polar residues present in more ancient organisms were eventually replaced by an isoleucine in later species. Based on sequence alignment (Fig. S1), a zS109 – zN120 -like interaction might have been present not only in bony fishes but already in the sea lamprey, a jawless vertebrate in which the ECL1 arginine did not yet appear, suggesting that it might represent an early stabilizing strategy. To address the timing of the evolutionary switch which eventually replaced that interaction with an H-bond between ECL6 and the ECL1 arginine, multiple CFTR orthologues would have to be studied both functionally and structurally, which is beyond the scope of the present study. Interestingly, the ancient

polar interaction must have been lost also in the course of evolution of the chondrichthyes branch, as extant cartilaginous fishes (e.g. sharks) also lack a polar residue at the position corresponding to zN120 (Fig. S1). Interestingly, the ancient polar interaction can be restored in the human orthologue by replacing the isoleucine with an asparagine (hI119N, Fig. 7).

Remarkably, despite the eventual loss of the zS109 – zN120 -like polar interaction, the serine has remained preserved throughout evolution (Fig. S1), and we show here that in hCFTR its presence is required for the open-state stabilization provided by the hR117 side chain (Fig. 6). Although the hS108-hR117 H-bond suggested by the OF hCFTR structure forms between the hR117 side chain and the backbone carbonyl group of hS108 (Fig. 4C), that structure also suggests that the serine side chain is important for positioning of its backbone, by stabilizing the last turn of the TM1 helix – this would explain the strong functional effect of the hS108A side chain truncation (Fig. 6). It is presently unclear whether the hS108-hR117 interaction is required for proper positioning of the arginine side chain to facilitate its interaction with ECL6-residue hE1124, or for extending the mechanical coupling from ECL6 to the C-terminal end of TM1, but it is clear that the simultaneous presence of both interactions is required for open-state stabilization in hCFTR (Fig. 8, lower panel).

Mutations of hR117 are the cause of CF for thousands of people. Interestingly, despite the disastrous impacts on CFTR gating of the hS108A mutation (Fig. 6), variations of hS108 are not registered in the CF database. There are several possible reasons to explain the lack of CF patients with such a mutation. First, serine is encoded by six codons and any replacement of the third base in the native codon of hS108 (TCT) is silent. Second, although the same is true for hR117, replacement of hS108 by other polar amino acids, such as threonine or asparagine, might preserve the native orientation of its backbone, whereas any replacement of the hR117 side chain will necessarily disrupt the ECL1-ECL6 H-bond, destabilizing the O state. Third, It is also possible that mutations of the serine residue are embryonic lethal.

The bursting gating pattern of CFTR might be explained by two linear three-state schemes: $C_s - C_f - O$ or $C_s - O - C_f$. To date no data exist that would allow distinction between these two possibilities In particular, the dependences of microscopic reaction

rates on ATP concentration (Winter *et al.*, 1994), pH (Chen *et al.*, 2017), or voltage (Cai *et al.*, 2003), as well as the effects of disrupting an interaction that selectively stabilizes the O state (Simon et al., 2021), are equally compatible with either model. Although in principle a distinction might be offered by mutations which either disrupt an interaction selectively present in the C_f state (cf., zN120A), or create a C_f-specific interaction (cf., hI119N), evaluation of the effects of these two mutations by fitting either scheme did not provide any strong bias. However, a slight preference for the $C_s - C_f - O$ scheme (Fig. 8) is supported by the state-dependence of the target interaction (z109-z120 native, h108-h119 in hI119N). Based on the mutant cycles (Figs. 5, 7) the H-bond forms in states C_f and $T^{\ddagger}$ for both orthologues. Whereas in the $C_s - C_f - O$ scheme those two states are directly linked, in the $C_s - O - C_f$ scheme they are separated.

In conclusion, we have pinpointed specific structural differences in ECL1 that are responsible for the functional differences between two distant CFTR orthologs. Our findings provide first insights into how CFTR gating mechanism was optimized in the course of CFTR molecular evolution.

Supplementary material

Supplementary material includes Figs. S1, S2, as referenced in the main text.

Acknowledgements

The zCFTR coding sequence was a generous gift of T. C. Hwang. Supported by EU Horizon 2020 Research and Innovation Program grant 739593, MTA Lendület grant LP2017-14/2017, and Cystic Fibrosis Foundation Research Grant CSANAD21G0 to LC. MAS received support from the ÚNKP-21–3-II-SE-19 New National Excellence Program of the Ministry for Innovation and Technology from the source of the National Research, Development and Innovation Fund.

Author contribution

MAS: Conceptualization, Formal analysis, Funding acquisition, Investigation, Software, Visualization, Writing – original draft. LCS: Data curation, Funding acquisition, Project

administration, Methodology, Software, Supervision, Validation, Writing – review & editing.

References

Bai,Y.H., M.Li, and T.C.Hwang. 2011. Structural basis for the channel function of a degraded ABC transporter, CFTR (ABCC7). *Journal of General Physiology* 138:495-507.

Barry,P.J., M.A.Mall, A.Ã lvarez, C.Colombo, de Winter-de Groot KM, I.Fajac, K.A.McBennett, E.F.Mckone, B.W.Ramsey, S.Sutharsan, J.L.Taylor-Cousar, E.Tullis, N.Ahluwalia, L.S.Jun, S.M.Moskowitz, V.Prieto-Centurion, S.Tian, D.Waltz, F.Xuan, Y.Zhang, S.M.Rowe, and D.Polineni. 2021. Triple Therapy for Cystic Fibrosis Phe508del-Gating and -Residual Function Genotypes. *N Engl J Med* 385:815-825.

Cai,Z., T.S.Scott-Ward, and D.N.Sheppard. 2003. Voltage-dependent gating of the cystic fibrosis transmembrane conductance regulator Cl- channel. *J Gen Physiol* 122:605-620.

Chen,J.H., W.Xu, and D.N.Sheppard. 2017. Altering intracellular pH reveals the kinetic basis of intraburst gating in the CFTR Cl- channel. *J Physiol* 595:1059-1076.

Cheng,S.H., D.P.Rich, J.Marshall, R.J.Gregory, M.J.Welsh, and A.E.Smith. 1991. Phosphorylation of the R domain by cAMP-dependent protein kinase regulates the CFTR chloride channel. *Cell* 66:1027-1036.

Csanády,L., P.Vergani, and D.C.Gadsby. 2010. Strict coupling between CFTR's catalytic cycle and gating of its Cl- ion pore revealed by distributions of open channel burst durations. *Proc Natl Acad Sci U S A* 107:1241-1246.

Csanády,L., P.Vergani, and D.C.Gadsby. 2019. STRUCTURE, GATING, AND REGULATION OF THE CFTR ANION CHANNEL. *Physiol Rev* 99:707-738.

Cui,G., J.Hong, Y.W.Chung-Davidson, D.Infield, X.Xu, J.Li, L.Simhaev, N.Khazanov, B.Stauffer, B.Imhoff, K.Cottrill, J.E.Blalock, W.Li, H.Senderowitz, E.Sorscher, N.A.McCarty, and A.Gaggar. 2019. An Ancient CFTR Ortholog Informs Molecular Evolution in ABC Transporters. *Dev Cell* 51:421-430.

Cui,G.Y., K.S.Rahman, D.T.Infield, C.Kuang, C.Z.Prince, and N.A.McCarty. 2014. Three charged amino acids in extracellular loop 1 are involved in maintaining the outer pore architecture of CFTR. *Journal of General Physiology* 144:159-179.

De Boeck,K. and M.D.Amaral. 2016. Progress in therapies for cystic fibrosis. *Lancet Respir Med* 4:662-674.

Dean,M., M.B.White, J.Amos, B.Gerrard, C.Stewart, K.T.Khaw, and M.Leppert. 1990. Multiple mutations in highly conserved residues are found in mildly affected cystic fibrosis patients. *Cell* 61:863-870.

Fersht,A. 2002. Structure and Mechanism in protein science. 4 ed. W.H.Freeman and Company, New York.

Heijerman,H.G.M., E.F.Mckone, D.G.Downey, E.Van Braeckel, S.M.Rowe, E.Tullis, M.A.Mall, J.J.Welter, B.W.Ramsey, C.M.McKee, G.Marigowda, S.M.Moskowitz, D.Waltz, P.R.Sosnay, C.Simard, N.Ahluwalia, F.Xuan, Y.Zhang, J.L.Taylor-Cousar, and K.S.McCoy. 2019. Efficacy and safety of the elexacaftor plus tezacaftor plus ivacaftor combination regimen in people with cystic fibrosis homozygous for the F508del mutation: a double-blind, randomised, phase 3 trial. *Lancet* 394:1940-1948.

Infield,D.T., G.Cui, C.Kuang, and N.A.McCarty. 2016. Positioning of extracellular loop 1 affects pore gating of the cystic fibrosis transmembrane conductance regulator. *Am J Physiol Lung Cell Mol Physiol* 310:L403-L414.

Infield,D.T., K.M.Strickland, A.Gaggar, and N.A.McCarty. 2021. The molecular evolution of function in the CFTR chloride channel. *J Gen Physiol* 153.

Liu,F., Z.Zhang, L.Csanády, D.C.Gadsby, and J.Chen. 2017. Molecular Structure of the Human CFTR Ion Channel. *Cell* 169:85-95.

Middleton,P.G., M.A.Mall, P.DÅ™evÃ-nek, L.C.Lands, E.F.Mckone, D.Polineni, B.W.Ramsey, J.L.Taylor-Cousar, E.Tullis, F.Vermeulen, G.Marigowda, C.M.McKee, S.M.Moskowitz, N.Nair, J.Savage, C.Simard, S.Tian, D.Waltz, F.Xuan, S.M.Rowe, and R.Jain. 2019. Elexacaftor-Tezacaftor-Ivacaftor for Cystic Fibrosis with a Single Phe508del Allele. *N Engl J Med* 381:1809-1819.

Mihályi,C., I.Iordanov, B.Töröcsik, and L.Csanády. 2020. Simple binding of protein kinase A prior to phosphorylation allows CFTR anion channels to be opened by nucleotides. *Proc Natl Acad Sci U S A* 117:21740-21746.

Mihályi,C., B.Torocsik, and L.Csanády. 2016. Obligate coupling of CFTR pore opening to tight nucleotide-binding domain dimerization. *Elife* 5. pii: e18164. doi: 10.7554/eLife.18164.:e18164.

O'Sullivan,B.P. and S.D.Freedman. 2009. Cystic fibrosis. *Lancet* 373:1891-1904.

Ramsey,B.W., J.Davies, N.G.McElvaney, E.Tullis, S.C.Bell, P.Drevinek, M.Griese, E.F.Mckone, C.E.Wainwright, M.W.Konstan, R.Moss, F.Ratjen, I.Sermet-Gaudelus, S.M.Rowe, Q.M.Dong, S.Rodriguez, K.Yen, C.Ordonez, and J.S.Elborn. 2011. A CFTR Potentiator in Patients with Cystic Fibrosis and the G551D Mutation. *New England Journal of Medicine* 365:1663-1672.

Riordan,J.R., J.M.Rommens, B.Kerem, N.Alon, R.Rozmahel, Z.Grzelczak, J.Zielenski, S.Lok, N.Plavsic, J.L.Chou, and . 1989. Identification of the cystic fibrosis gene: cloning and characterization of complementary DNA. *Science* 245:1066-1073.

Sheppard,D.N., D.P.Rich, L.S.Ostedgaard, R.J.Gregory, A.E.Smith, and M.J.Welsh. 1993. Mutations in CFTR associated with mild-disease-form Cl- channels with altered pore properties. *Nature* 362:160-164.

Simon,M.A. and L.Csanády. 2021. Molecular pathology of the R117H cystic fibrosis mutation is explained by loss of a hydrogen bond. *Elife* 10.

Sutharsan,S., E.F.Mckone, D.G.Downey, J.Duckers, G.MacGregor, E.Tullis, E.Van Braeckel, C.E.Wainwright, D.Watson, N.Ahluwalia, B.G.Bruinsma, C.Harris, A.P.Lam, Y.Lou, S.M.Moskowitz, S.Tian, J.Yuan, D.Waltz, and M.A.Mall. 2022. Efficacy and safety of elexacaftor plus tezacaftor plus ivacaftor versus tezacaftor plus ivacaftor in people with cystic fibrosis homozygous for F508del-CFTR: a 24-week, multicentre, randomised, double-blind, active-controlled, phase 3b trial. *Lancet Respir Med* 10:267-277.

Tsai,M.F., M.Li, and T.C.Hwang. 2010. Stable ATP binding mediated by a partial NBD dimer of the CFTR chloride channel. *J Gen Physiol* 135:399-414.

Vergani,P., S.W.Lockless, A.C.Nairn, and D.C.Gadsby. 2005. CFTR channel opening by ATP-driven tight dimerization of its nucleotide-binding domains. *Nature* 433:876-880.

Wang,W., B.C.Roessler, and K.L.Kirk. 2014. An Electrostatic Interaction at the Tetrahelix Bundle Promotes Phosphorylation-dependent Cystic Fibrosis Transmembrane Conductance Regulator (CFTR) Channel Opening. *Journal of Biological Chemistry* 289:30364-30378.

Wilschanski,M., J.Zielenski, D.Markiewicz, L.C.Tsui, M.Corey, H.Levison, and P.R.Durie. 1995. Correlation of sweat chloride concentration with classes of the cystic fibrosis transmembrane conductance regulator gene mutations. *J Pediatr* 127:705-710.

Winter,M.C., D.N.Sheppard, M.R.Carson, and M.J.Welsh. 1994. Effect of ATP concentration on CFTR Cl- channels: a kinetic analysis of channel regulation. *Biophys J* 66:1398-1403.

Yu,Y.C., Y.Sohma, and T.C.Hwang. 2016. On the mechanism of gating defects caused by the R117H mutation in cystic fibrosis transmembrane conductance regulator. *J Physiol* 594:3227-3244.

Zhang,J., Y.C.Yu, J.T.Yeh, and T.C.Hwang. 2018a. Functional characterization reveals that zebrafish CFTR prefers to occupy closed channel conformations. *PLoS One* 13:e0209862.

Zhang,Z. and J.Chen. 2016. Atomic Structure of the Cystic Fibrosis Transmembrane Conductance Regulator. *Cell* 167:1586-1597.

Zhang,Z., F.Liu, and J.Chen. 2017. Conformational Changes of CFTR upon Phosphorylation and ATP Binding. *Cell* 170:483-491.

Zhang,Z., F.Liu, and J.Chen. 2018b. Molecular structure of the ATP-bound, phosphorylated human CFTR. *Proc Natl Acad Sci U S A.*

Abbreviations

z/h CFTR – zebrafish / human cystic fibrosis transmembrane conductance regulator; CF – cystic fibrosis; IF – inward-facing; OF – outward-facing; TMD1/2 – transmembrane domain 1/2; NBD1/2 – nucleotide binding domain 1/2; R domain – regulatory domain, ECL – extracellular loop; TM – transmembrane helix; B state – burst state; O state – open state; IB state – interburst closed state; C_f state – flickery closed state; C_s state – C slow closed state; $T^{\ddagger}$ state – transition state.

Figure legends

Fig. 1. The stabilizing H-bond present in the phosphorylated ATP bound (outward-facing, OF) hCFTR structure, but is absent in the phosphorylated, ATP-bound (OF) zCFTR structure.

(A) Cartoon topology of CFTR ion channel and location of hR117/zR118 and hE1124/zD1132 residues (blue / pale blue and brown dot). TMDs, gray; NBD1, blue; NBD2, green; R domain, pale magenta; membrane, yellow. Catalytic site mutation in the NBD2 Walker B motif is represented by a pale green star. (B-C) Ribbon diagrams of the OF hCFTR (PDB: 6msm) (B) and OF zCFTR (PDB: 5w81) (C) cryo-EM structures, highlighting residues hR117/zR118 (blue / pale blue) and hE1124/zD1132 (brown) in space fill representation. TMDs and NBDs are color coded as in A, R domain is not depicted. (D–E) Close-up views of the extracellular region highlighted in B and C by dotted purple boxes. Residues hR117/zR118 and hE1124/zD1132 are shown as sticks, the H-bond in OF hCFTR is illustrated by red dotted lines with bond distance marked, TM helices (TM1, TM2) are assigned.

Fig. 2. The mean duration of non-hydrolytic bursts (τ_{burst}) is similar but the intraburst equilibrium constant ($K_{eq|B}$) is much lower for zE1372S compared to hE1371S.

(A) Macroscopic current relaxations induced by ATP removal for the non-hydrolytic hE1371S (black) and zE1372S (gray) constructs. Inside-out patch currents were activated by exposure of pre-phosphorylated channels to 2 mM ATP. Membrane potential (V_m) was –20 and -40 mV for the zCFTR and hCFTR traces, respectively. Current amplitudes were rescaled by their initial values. (B) Relaxation time constants (τ_{burst}) of the currents

in A, obtained by fits to single exponentials for hE1371S (n = 7) and zE1372S (n = 9), n values refer to biological replicates. Data are shown as mean ± SEM, τ_{burst} values are not significantly different (p = 0.071). (C) Currents of last open channels after ATP removal, for the non-hydrolytic hE1371S (black) and zE1372S (gray) constructs. Inside-out patch currents were activated by exposure of pre-phosphorylated channels to 2 mM ATP. Membrane potential was -80 and -120 mV for hCFTR and zCFTR, respectively. Black lines indicate the analyzed segments. (D) Intraburst equilibrium constants ($K_{eq|B}$, see Materials and methods) of hE1371S (n = 6) and zE1372S (n = 12), plotted on a logarithmic scale (n values refer to biological replicates). Data are shown as mean ± SEM. SEM was calculated by uncertainty propagation.

Fig. 3. Dependency of non-hydrolytic mean burst duration on membrane composition and catalytic-site mutation for the two CFTR orthologues

(A, C) ATP removal-induced macroscopic current relaxations of the indicated h/zCFTR constructs in the indicated expression systems (color coded). Recordings were performed as described in Fig. 2. Membrane potential was -40 mV for hE1371S – oocyte/HEK293 and zE1372S-HEK293; and –20 mV for all other traces (zE1372S-oocyte, hE1371Q, zE1372Q), and current amplitudes were rescaled by their initial values. (B,D) Relaxation time constants (τ_{burst}) of the currents in A and C, obtained by fits to single exponentials for hE1371S expressed in *Xenopus* oocytes (n = 7), hE1371S expressed in HEK293T cells (n = 7), zE1372S expressed in *Xenopus* oocytes (n = 9), zE1372S expressed in HEK293T cells (n = 7), hE1371Q expressed in *Xenopus* oocytes (n = 4) and zE1372Q expressed in *Xenopus* oocytes (n = 6), n values refer to biological replicates. Data are shown as mean ± SEM. The τ_{burst} values of zE1372S and zE1372Q are not significantly different (p = 0.092). The differences between τ_{burst} values in the two expression systems were significant neither for hE1371S (p=0.42), nor for zE1372S (p=0.091)

Fig. 4. The zR118H zebrafish CFTR mutant exhibits no hR117H-like phenotype

(A) ATP removal-induced macroscopic current relaxations of the indicated h/zCFTR mutants (color coded). Recordings were performed as described in Fig. 2. Membrane potential was -20 mV for zCFTR and -40 mV for hCFTR orthologues and current amplitudes were rescaled by their initial values. (B) Relaxation time constants (τ_{burst}) of

the currents in A, obtained by fits to single exponentials for hE1371S (n = 6), hR117H (N = 8), zE1372S (n = 7) and zR118H (n = 7), n values refer to biological replicates. Data are shown as mean ± SEM. The τ_{burst} values of zE1372S and zE1372S–R118H are not significantly different (p = 0.27) (C-F) Close-up views of the extracellular region near hR117/zR118 for the OF (C-D) and IF (E-F) structures for both orthologues. Residues hR117/zR118, hE1124/zD1132, hS108/zS109 and hI119/zN120 are shown as sticks, H-bonds in OF hCFTR and zCFTR are illustrated by red dotted lines with bond distances marked, TM helices (TM1, TM2) are assigned.

Fig. 5. The H-bond between zS109 and zN120 is present only in the C_f state

(A) Currents of last open channels after ATP removal of the indicated zCFTR mutants (color coded). Recordings were done as described for Fig 2. Membrane potential was -120 mV. Black lines indicate the analyzed segments. (B) Intraburst equilibrium constants ($K_{eq|B}$) of zE1372S (n = 5), zN120A (n = 5), zS109A (n = 6) and zS109A-N120A (n = 8), plotted on a logarithmic scale, n values refer to biological replicates. Data are shown as mean ± SEM. SEM was calculated by uncertainty propagation. (C, F) Thermodynamic mutant cycles showing mutation-induced changes in the stability of the O state relative to the C_f state (C) or of the $T^{\ddagger}$ state relative to the B state (F) ($\Delta\Delta G^0_{O\text{-}Cf}$ and $\Delta\Delta G^0_{T\ddagger\text{-}B}$, numbers on arrows; k, Boltzmann's constant; T, absolute temperature). Each corner of the cycle is represented by the mutations introduced into positions zS109 and zN120 of zE1372S. $\Delta\Delta G_{int}$ (purple number) is obtained as the difference between $\Delta\Delta G^0$ values along two parallel sides of the cycle. (D) ATP removal-induced macroscopic current relaxations of the indicated zCFTR mutants (color coded). Recordings were executed as described in Fig. 2. Membrane potential was -20 mV for the background construct, -40 mV for the single mutants, and -80 mV for the double mutant. Current amplitudes were rescaled by their initial values. (E) Relaxation time constants (τ_{burst}) of the currents in D, obtained by fits to single exponentials for zE1372S (n = 7), zN120A (n = 6), zS109A (n = 7) and zS109A-N120A (n = 7), n values refer to biological replicates. Data are shown as mean ± SEM.

Fig. 6. In hCFTR, hS108 interacts with hR117 in the open state.

(A) ATP removal-induced macroscopic current relaxations of the indicated hCFTR mutants (color coded). Recordings were executed as described in Fig. 2. Membrane potential was -40 mV for the background and the single mutants, and -80 mV for the double mutant and current amplitudes were rescaled by their initial values. (B) Relaxation time constants (τ_{burst}) of the currents in A, obtained by fits to single exponentials for hE1371S (n = 6), hS108A (n = 9), hR117H (n = 8) and hS108A-R117H (n = 9), n values refer to biological replicates. Data are shown as mean ± SEM. (C, F) Thermodynamic mutant cycles showing mutation-induced changes in the stability of the $T^{‡}$ state relative to the B state (C) or of the O state relative to the C_f state (F) ($\Delta\Delta G^0_{T‡\text{-}B}$ and $\Delta\Delta G^0_{O\text{-}Cf}$, numbers on arrows; k, Boltzmann's constant; T, absolute temperature). Each corner of the cycle is represented by the mutations introduced into positions hS108 and hR117 of hE1371S. $\Delta\Delta G_{int}$ (purple number) is obtained as the difference between $\Delta\Delta G^0$ values along two parallel sides of the cycle. (D) Currents of last open channels after ATP removal of the indicated hCFTR mutants (color coded). Recordings were done as described in Fig 2. Membrane potential was -80 mV. Black lines indicate the analyzed segments. (E) Intraburst equilibrium constants ($K_{eq|B}$) of hE1371S (n = 5), hS108A (n = 7), hR117H (n = 8) and hS108A-R117H (n = 6), plotted on a logarithmic scale, n values refer to biological replicates. Data are shown as mean ± SEM. SEM was calculated by uncertainty propagation.

Fig. 7. The hS108-I119N interaction stabilizes the C_f state in hCFTR

(A) Currents of last open channels after ATP removal of the indicated hCFTR mutants (color coded). Recordings were done as described in Fig 2. Membrane potential was -80 mV for the background and the single mutants, and -120 mV for the double mutant. Black lines indicate the analyzed segments. (B) Intraburst equilibrium constants ($K_{eq|B}$) of hE1371S (n = 5), hS108A (n = 7), hI119N (n = 9) and hS108A-I119N (n = 7), plotted on a logarithmic scale, n values refer to biological replicates. Data are shown as mean ± SEM. SEM was calculated by uncertainty propagation. (C,F) Thermodynamic mutant cycles showing mutation-induced changes in the stability of the O state relative to the C_f state (C) or of the $T^{‡}$ state relative to the B state (F) ($\Delta\Delta G^0_{O\text{-}Cf}$ and $\Delta\Delta G^0_{T‡\text{-}B}$, numbers on arrows; k, Boltzmann's constant; T, absolute temperature). Each corner of the cycle is

represented by the mutations introduced into positions hS108 and hI119 of hE1371S. $\Delta\Delta G_{int}$ (purple number) is obtained as the difference between $\Delta\Delta G^0$ values along two parallel sides of the cycle. (D) ATP removal-induced macroscopic current relaxations of the indicated hCFTR mutants (color coded). Recordings were executed as described in Fig. 2. Membrane potential was -40 mV for the background and the single mutants, and -80 mV for the double mutant. Current amplitudes were rescaled by their initial values. (E) Relaxation time constants (τ_{burst}) of the currents in D, obtained by fits to single exponentials for hE1371S (n = 6), hS108A (n = 9), hI119N (n = 8) and hS108A-I119N (n = 8), n values refer to biological replicates. Data are shown as mean ± SEM.

Fig. 8. Molecular evolution of stabilizing interactions between extracellular loops of CFTR

Cartoon model of the extracellular region (including TM1-ECL1-TM2 and TM11-ECL6-TM12) of CFTR orthologues representing C_s, C_f and O states, drawn in the framework of the $C_s - C_f - O$ mechanism. Color coding as in Figs 1 and 3. Target residues are shown as colored circles, H-bonds are represented by red dotted lines. Question mark denotes the unknown residue in zCFTR which stabilizes the O state by bonding to zS109.

Tables

	τ_{burst} (s)	**τ_{open} (ms)**	**$\tau_{flickery}$ (ms)**	**$K_{eq|B}$**
zE1372S	57 ± 8.3 (9)	19 ± 3.6	55 ± 8.0	0.35 ± 0.079 (12)
zE1372Q	78 ± 6.7 (6)	n.d.	n.d.	n.d.
zS109A	19 ± 3.0 (7)	14 ± 3.3	150 ± 32	0.094 ± 0.027 (9)
zN120A	40 ± 7.7 (6)	37 ± 6.2	14 ± 1.5	2.6 ± 0.51 (5)
zS109A-N120A	13 ± 0.82 (7)	9.0 ± 1.5	200 ± 31	0.045 ± 0.0094 (12)
zR118H	72 ± 11 (7)	n.d.	n.d.	n.d.
zS109A-R118H	36 ± 3.4 (7)	n.d.	n.d.	n.d.
hE1371S	37 ± 3.7 (7)	200 ± 23	10 ± 2.2	19 ± 4.1 (6)
hE1371Q	470 ± 65 (4)	n.d.	n.d.	n.d.

hS108A	11 ± 1.4 (9)	33 ± 2.8	120 ± 16	0.27 ± 0.041 (7)
hI119N	50 ± 7.9 (8)	66 ± 5.8	61 ± 8.6	1.1 ± 0.17 (9)
hS108A-I119N	29 ± 5.0 (8)	19 ± 3.6	260 ± 39	0.074 ± 0.017 (7)
hR117H	9.5 ± 0.73 (8)	11 ± 2.1	150 ± 24	0.072 ± 0.018 (8)
hS108A-R117H	19 ± 2.4 (9)	5.4 ± 1.5	300 ± 38	0.018 ± 0.0054 (6)

Table 1 Model-independent descriptive parameters for the indicated mutant z/hCFTR constructs.

Gating parameters were obtained from macroscopic current relaxation and last open-channel recordings. Data are displayed as mean ± SEM, numbers of independent biological replicates are given in parentheses.

Fig. 1

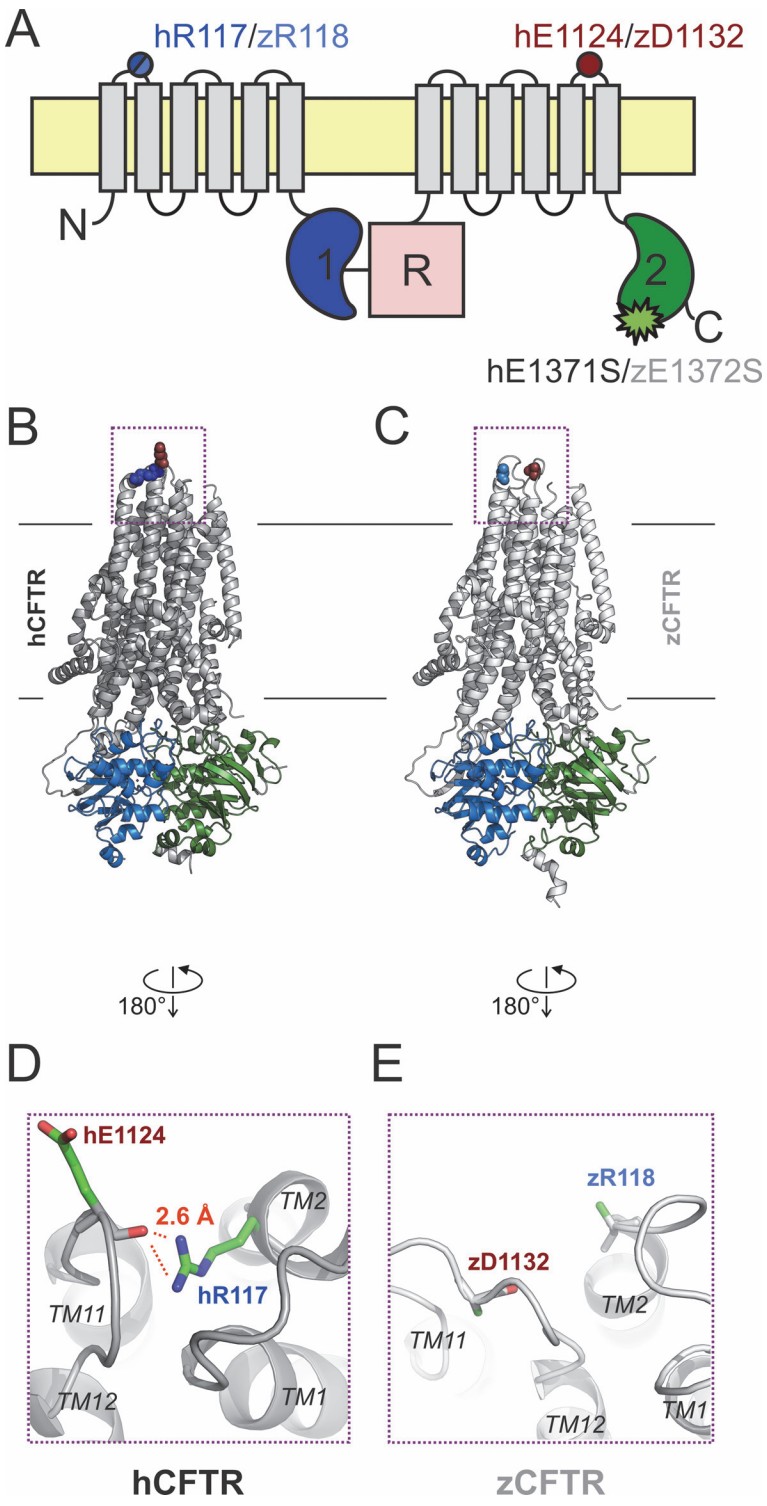
A
hR117/zR118
hE1124/zD1132
N
1
R
2
C
hE1371S/zE1372S
B
C
hCFTR
zCFTR
180°
180°
D
E
hE1124
2.6 Å
TM2
hR117
TM11
TM12
TM1
zR118
zD1132
TM2
TM11
TM12
TM1
hCFTR
zCFTR

Fig. 2

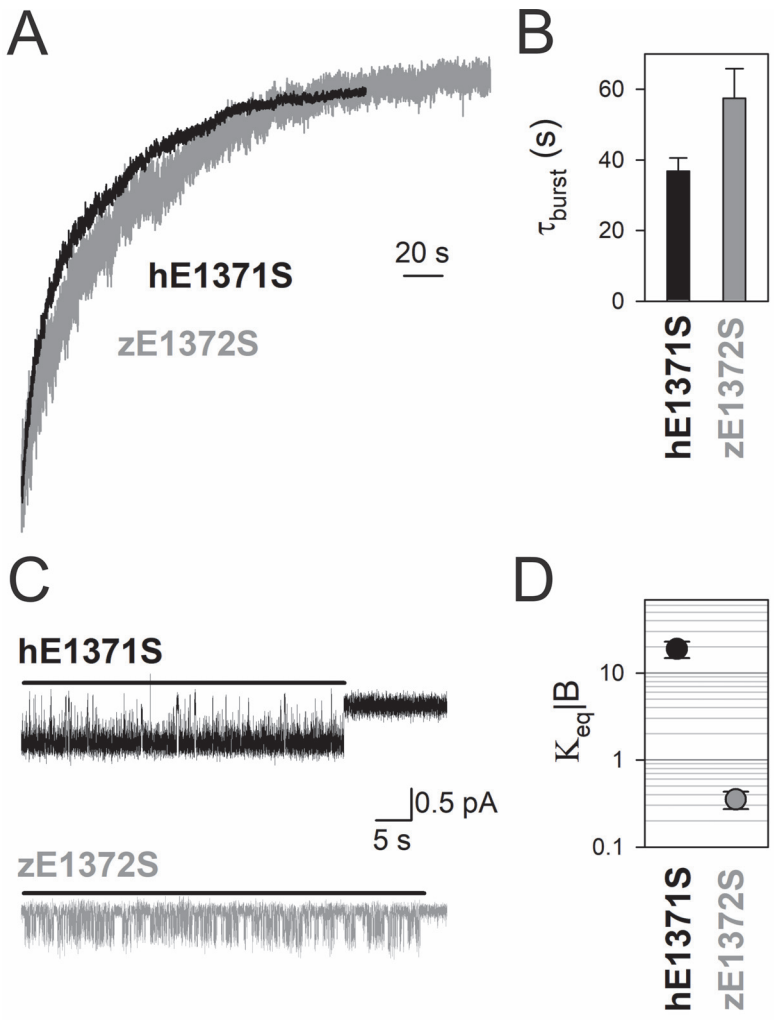
A
hE1371S
zE1372S
20 s
B
60
40
20
0
τ_{burst} (s)
hE1371S
zE1372S
C
hE1371S
0.5 pA
5 s
zE1372S
D
10
1
0.1
$K_{eq}|B$
hE1371S
zE1372S

Fig. 3

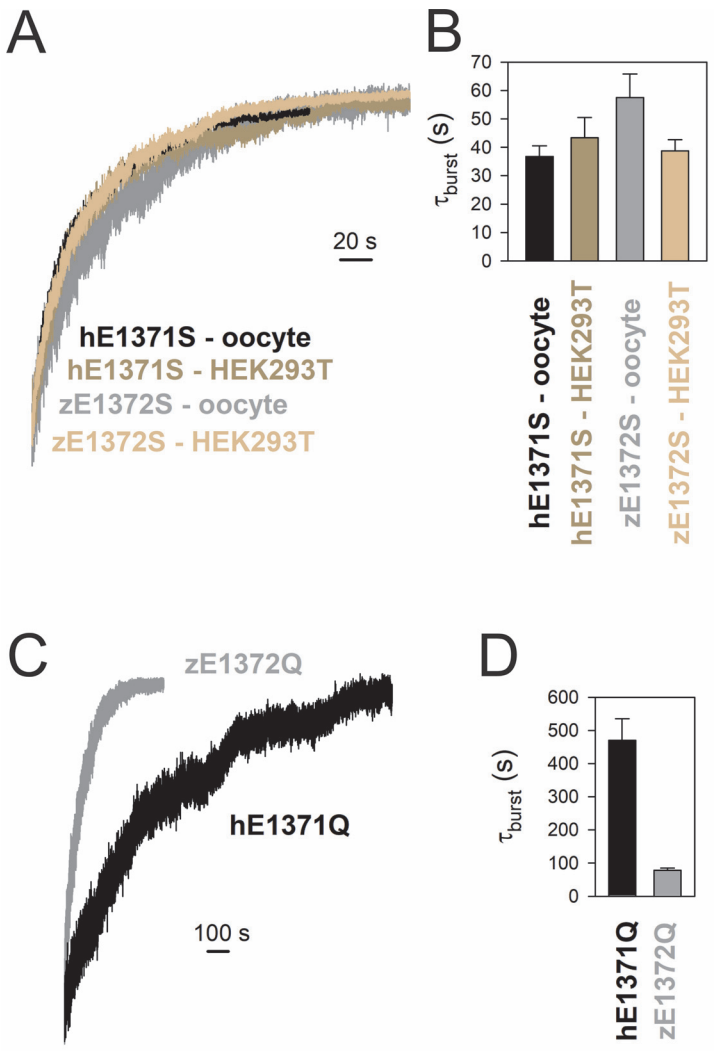
A
20 s
hE1371S - oocyte
hE1371S - HEK293T
zE1372S - oocyte
zE1372S - HEK293T
B
τburst (s)
70
60
50
40
30
20
10
0
hE1371S - oocyte
hE1371S - HEK293T
zE1372S - oocyte
zE1372S - HEK293T
C
zE1372Q
hE1371Q
100 s
D
τburst (s)
600
500
400
300
200
100
0
hE1371Q
zE1372Q

Fig. 4

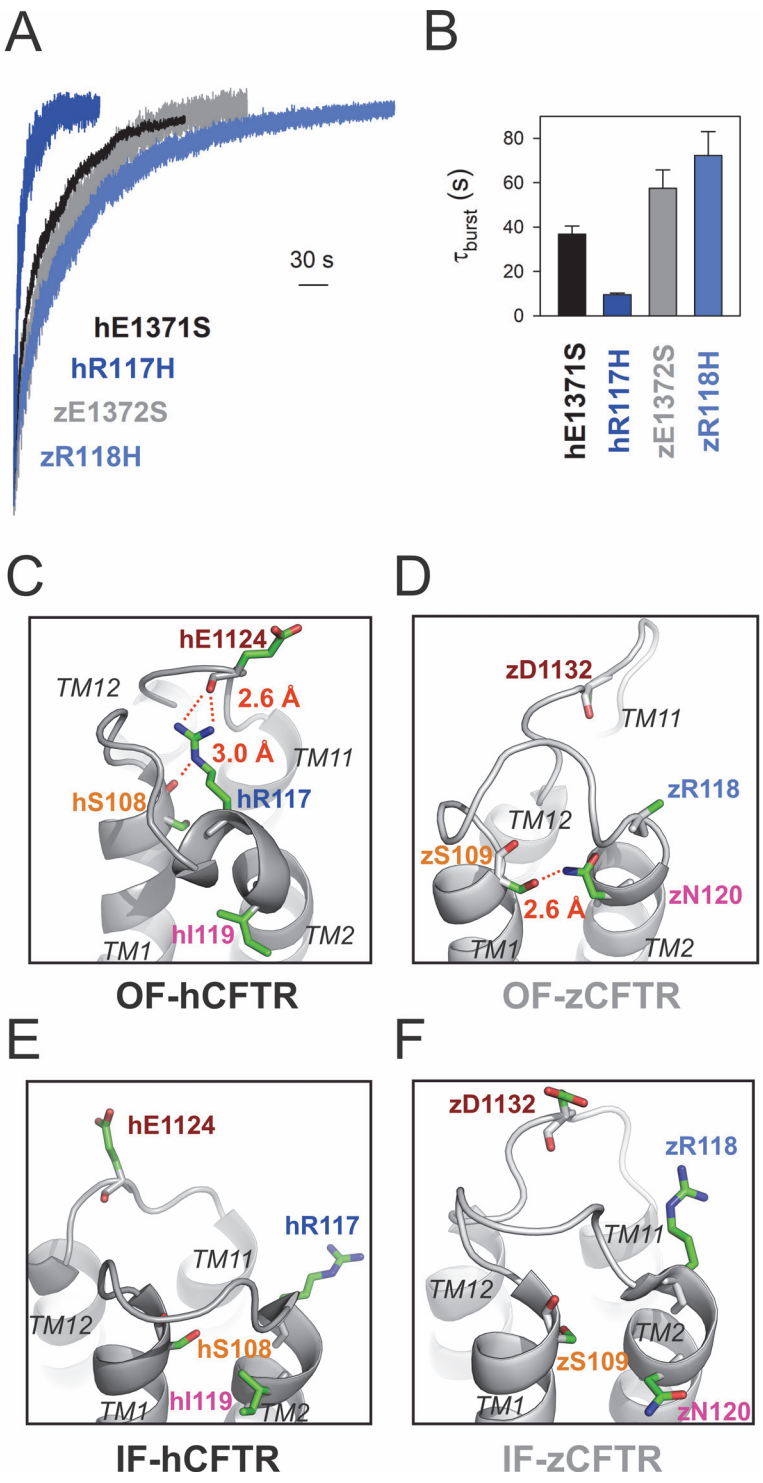
A
30 s
hE1371S
hR117H
zE1372S
zR118H
B
τ_{burst} (s)
80
60
40
20
0
hE1371S
hR117H
zE1372S
zR118H
C
hE1124
TM12
2.6 Å
3.0 Å
TM11
hS108
hR117
TM1
hI119
TM2
OF-hCFTR
D
zD1132
TM11
zR118
TM12
zS109
2.6 Å
zN120
TM1
TM2
OF-zCFTR
E
hE1124
hR117
TM11
TM12
hS108
TM1
hI119
TM2
IF-hCFTR
F
zD1132
zR118
TM11
TM12
TM2
zS109
TM1
zN120
IF-zCFTR

Fig. 5

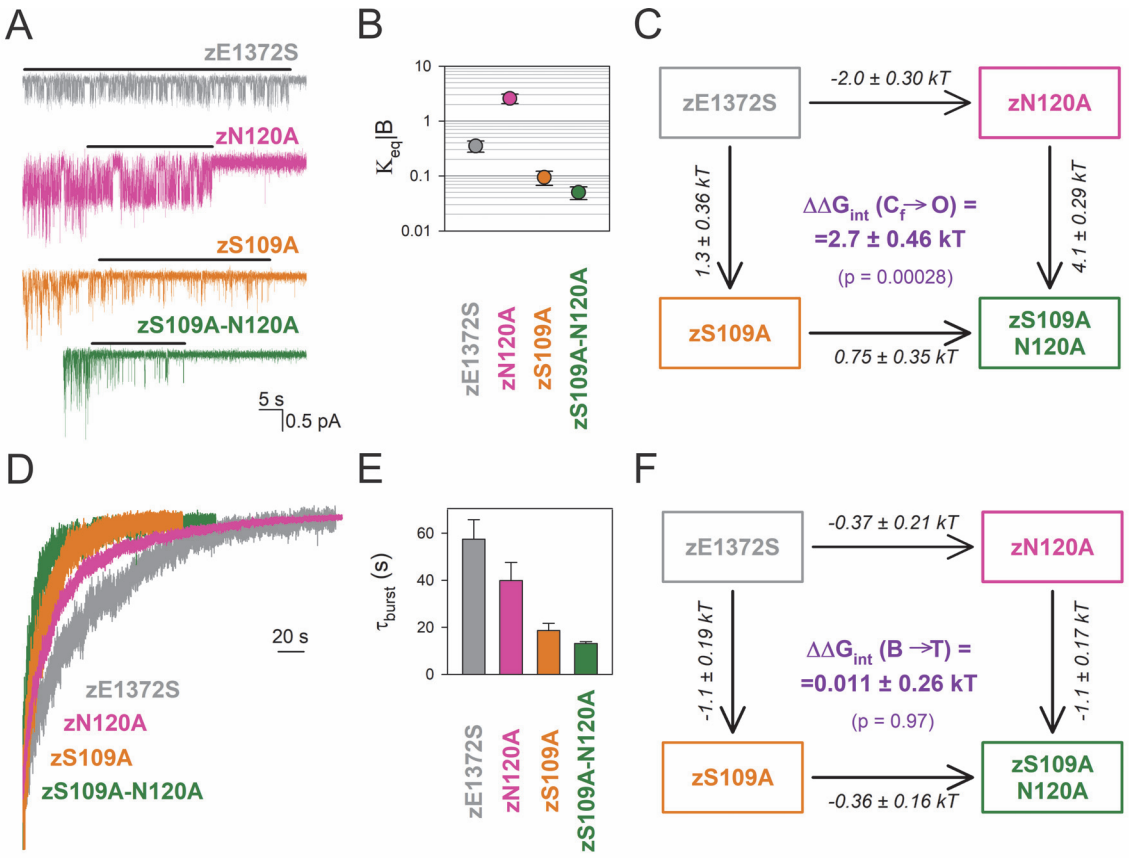
A
zE1372S
zN120A
zS109A
zS109A-N120A
5 s
0.5 pA
B
K_{eq}|B
10
1
0.1
0.01
zE1372S
zN120A
zS109A
zS109A-N120A
C
zE1372S
-2.0 ± 0.30 kT
zN120A
1.3 ± 0.36 kT
ΔΔG$_{int}$ (C$_f$→O) =
=2.7 ± 0.46 kT
(p = 0.00028)
4.1 ± 0.29 kT
zS109A
0.75 ± 0.35 kT
zS109A
N120A
D
20 s
zE1372S
zN120A
zS109A
zS109A-N120A
E
τ_{burst} (s)
60
40
20
0
zE1372S
zN120A
zS109A
zS109A-N120A
F
zE1372S
-0.37 ± 0.21 kT
zN120A
-1.1 ± 0.19 kT
ΔΔG$_{int}$ (B →T) =
=0.011 ± 0.26 kT
(p = 0.97)
-1.1 ± 0.17 kT
zS109A
-0.36 ± 0.16 kT
zS109A
N120A

Fig. 6

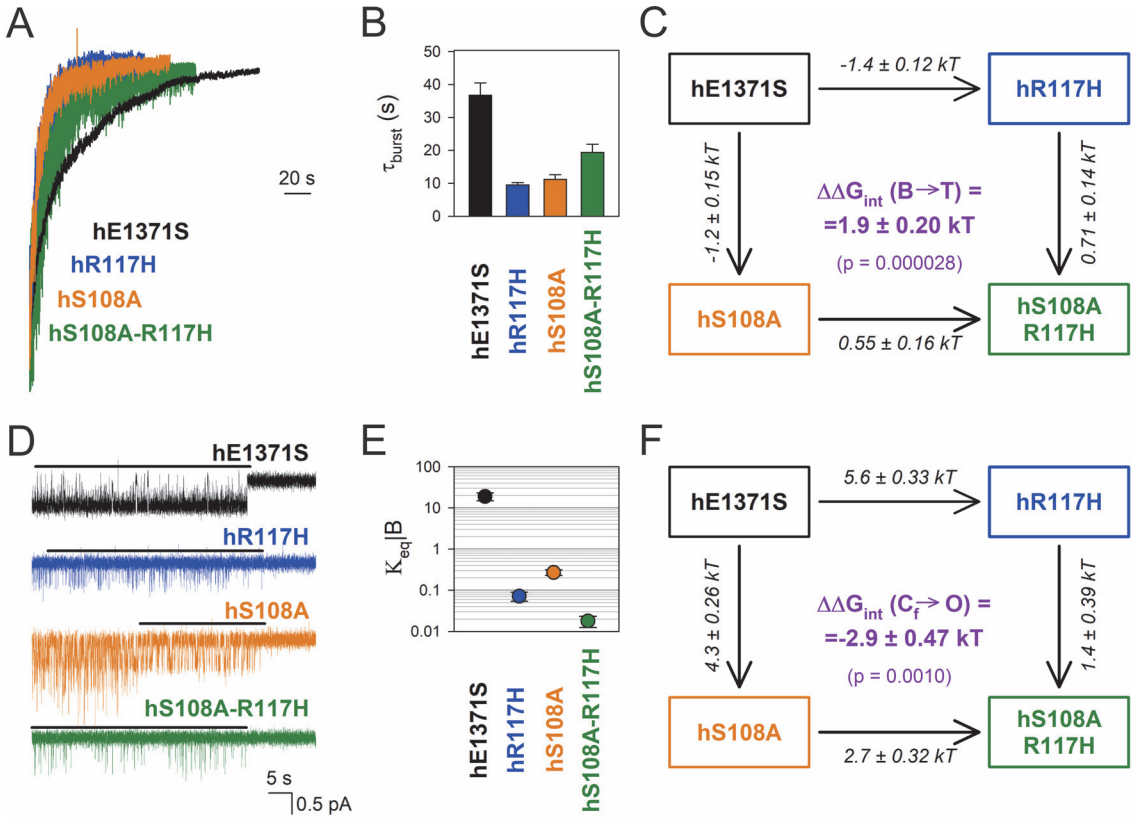
A
20 s
hE1371S
hR117H
hS108A
hS108A-R117H
B
τburst (s)
50
40
30
20
10
0
hE1371S
hR117H
hS108A
hS108A-R117H
C
hE1371S
-1.4 ± 0.12 kT
hR117H
-1.2 ± 0.15 kT
ΔΔGint (B→T) =
=1.9 ± 0.20 kT
(p = 0.000028)
0.71 ± 0.14 kT
hS108A
0.55 ± 0.16 kT
hS108A
R117H
D
hE1371S
hR117H
hS108A
hS108A-R117H
5 s
0.5 pA
E
Keq|B
100
10
1
0.1
0.01
hE1371S
hR117H
hS108A
hS108A-R117H
F
hE1371S
5.6 ± 0.33 kT
hR117H
4.3 ± 0.26 kT
ΔΔGint (Cf→ O) =
=-2.9 ± 0.47 kT
(p = 0.0010)
1.4 ± 0.39 kT
hS108A
2.7 ± 0.32 kT
hS108A
R117H

Fig. 7

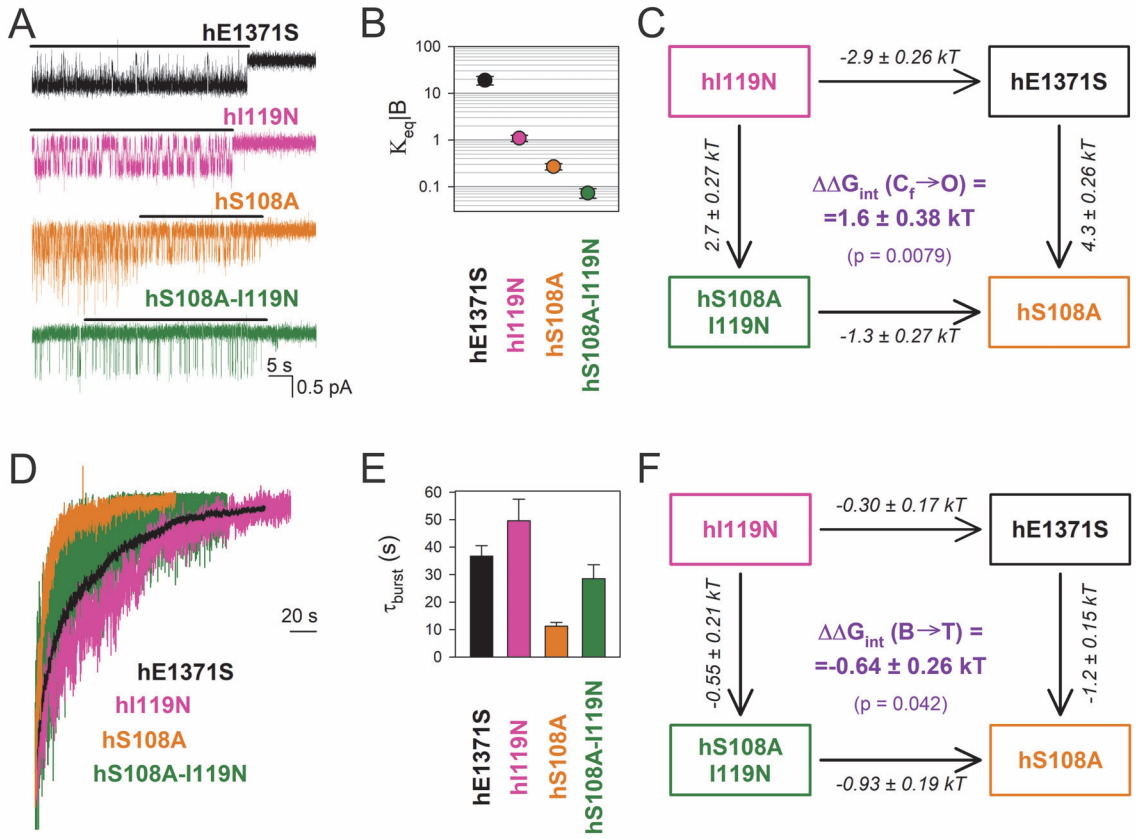
A
hE1371S
hI119N
hS108A
hS108A-I119N
5 s
0.5 pA
B
100
10
1
0.1
K_eq|B
hE1371S
hI119N
hS108A
hS108A-I119N
C
hI119N
-2.9 ± 0.26 kT
hE1371S
2.7 ± 0.27 kT
ΔΔG_int (C_f→O) =
=1.6 ± 0.38 kT
(p = 0.0079)
4.3 ± 0.26 kT
hS108A
I119N
-1.3 ± 0.27 kT
hS108A
D
20 s
hE1371S
hI119N
hS108A
hS108A-I119N
E
60
50
40
30
20
10
0
τ_burst (s)
hE1371S
hI119N
hS108A
hS108A-I119N
F
hI119N
-0.30 ± 0.17 kT
hE1371S
-0.55 ± 0.21 kT
ΔΔG_int (B→T) =
=-0.64 ± 0.26 kT
(p = 0.042)
-1.2 ± 0.15 kT
hS108A
I119N
-0.93 ± 0.19 kT
hS108A

Fig. 8

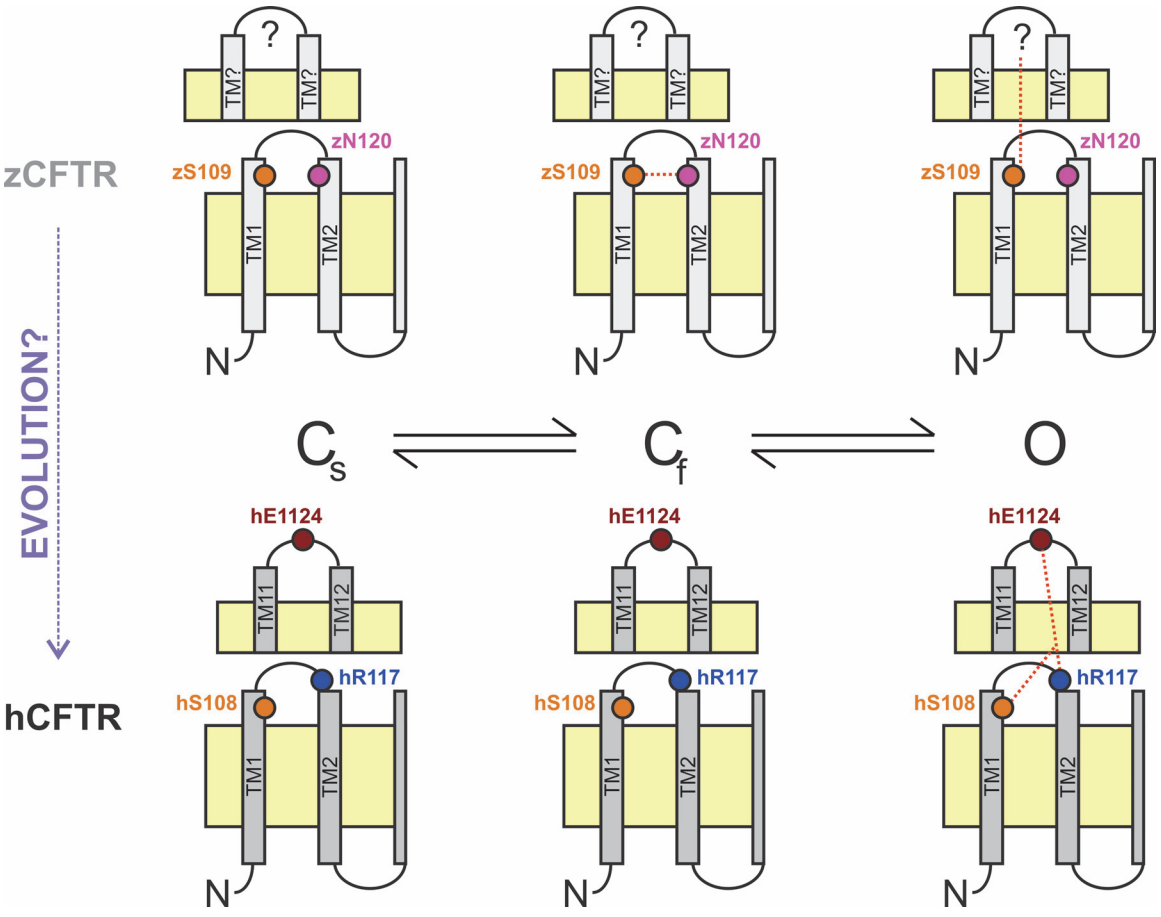
zCFTR
EVOLUTION?
hCFTR
TM?
zN120
zS109
TM1
TM2
N
Cs
Cf
O
hE1124
TM11
TM12
hR117
hS108

Fig. S1

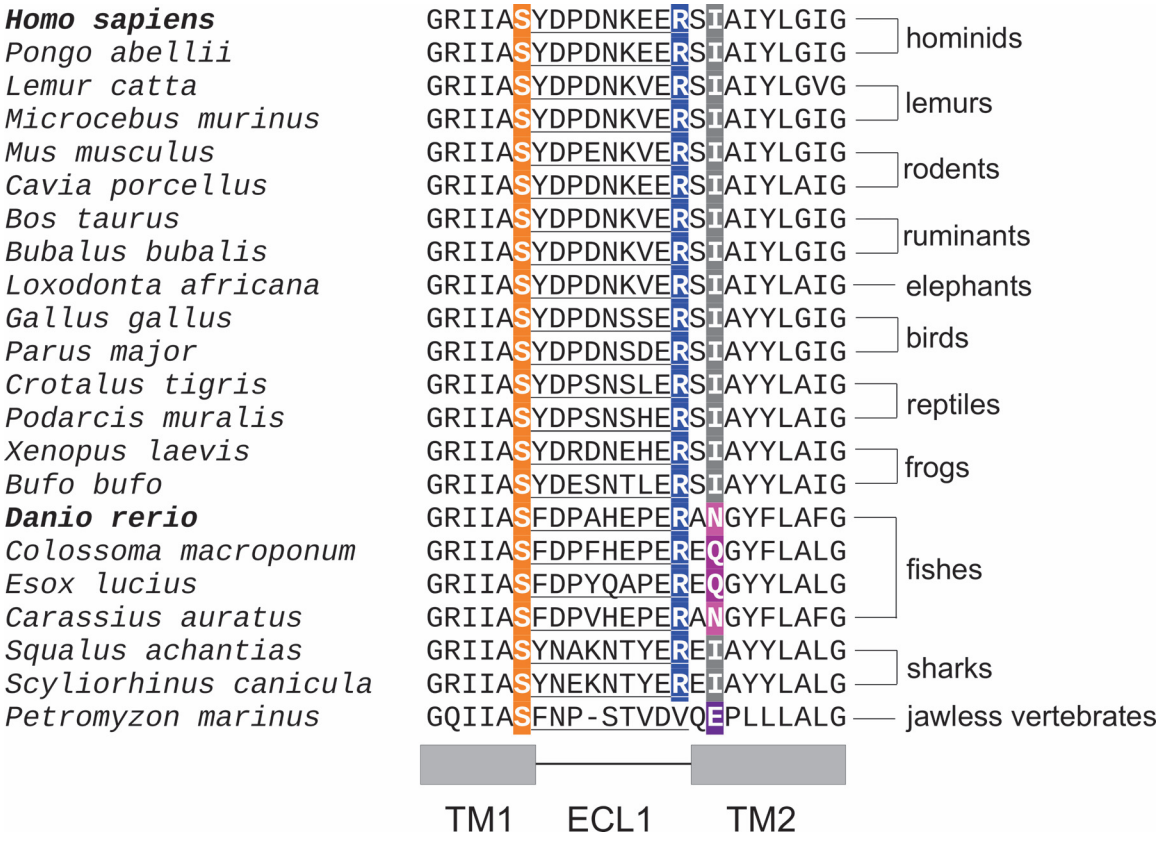
Homo sapiens GRIIASYDPDNKEERSIAIYLGIG
Pongo abellii GRIIASYDPDNKEERSIAIYLGIG
Lemur catta GRIIASYDPDNKVERSIAIYLGVG
Microcebus murinus GRIIASYDPDNKVERSIAIYLGIG
Mus musculus GRIIASYDPENKVERSIAIYLGIG
Cavia porcellus GRIIASYDPDNKEERSIAIYLAIG
Bos taurus GRIIASYDPDNKVERSIAIYLGIG
Bubalus bubalis GRIIASYDPDNKVERSIAIYLGIG
Loxodonta africana GRIIASYDPDNKVERSIAIYLAIG
Gallus gallus GRIIASYDPDNSSERSIAYYLGIG
Parus major GRIIASYDPDNSDERSIAYYLGIG
Crotalus tigris GRIIASYDPSNSLERSIAYYLAIG
Podarcis muralis GRIIASYDPSNSHERSIAYYLAIG
Xenopus laevis GRIIASYDRDNEHERSIAYYLAIG
Bufo bufo GRIIASYDESNTLERSIAYYLAIG
Danio rerio GRIIASFDPAHEPERANGYFLAFG
Colossoma macroponum GRIIASFDPFHEPEREQGYFLALG
Esox lucius GRIIASFDPYQAPEREQGYYLALG
Carassius auratus GRIIASFDPVHEPERANGYFLAFG
Squalus achantias GRIIASYNAKNTYERETAYYLALG
Scyliorhinus canicula GRIIASYNEKNTYERETAYYLALG
Petromyzon marinus GQIIASFNP-STVDVQEPLLLALG
hominids
lemurs
rodents
ruminants
elephants
birds
reptiles
frogs
fishes
sharks
jawless vertebrates
TM1
ECL1
TM2

Fig. S2

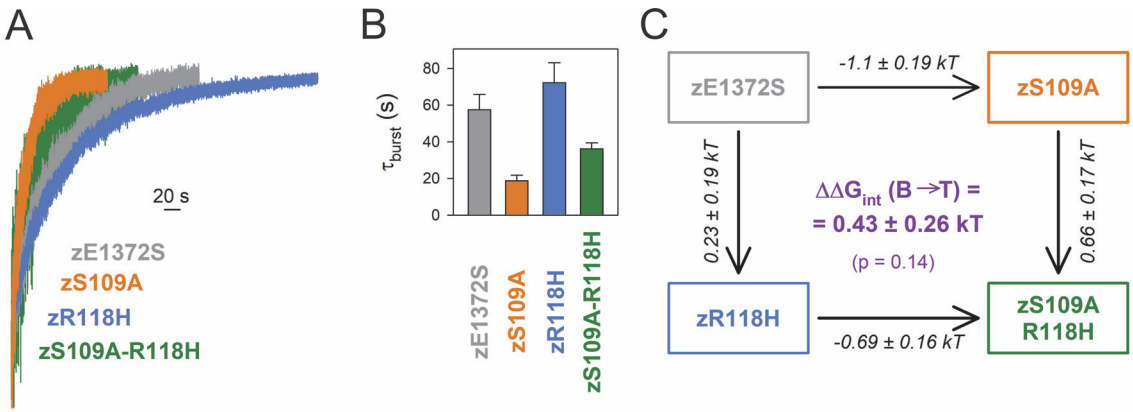
A
20 s
zE1372S
zS109A
zR118H
zS109A-R118H
B
τburst (s)
80
60
40
20
0
zE1372S
zS109A
zR118H
zS109A-R118H
C
zE1372S
-1.1 ± 0.19 kT
zS109A
0.23 ± 0.19 kT
ΔΔGint (B →T) =
= 0.43 ± 0.26 kT
(p = 0.14)
0.66 ± 0.17 kT
zR118H
-0.69 ± 0.16 kT
zS109A
R118H